

Structure symmetry determination and magnetic evolution in $\text{Sr}_2\text{Ir}_{1-x}\text{Rh}_x\text{O}_4$

Feng Ye,^{1,2} Xiaoping Wang,³ Christina Hoffmann,³ Jinchen Wang,^{1,2,4} Songxue Chi,¹ Masaaki Matsuda,¹ Bryan C. Chakoumakos,¹ Jaime A. Fernandez-Baca,^{1,5} and G. Cao²

¹Quantum Condensed Matter Division, Oak Ridge National Laboratory, Oak Ridge, Tennessee 37831, USA

²Center for Advanced Materials, Department of Physics and Astronomy, University of Kentucky, Lexington, Kentucky 40506, USA

³Chemical and Engineering Materials Division, Oak Ridge National Laboratory, Oak Ridge, Tennessee 37831, USA

⁴Department of Physics, Renmin University of China, Beijing 100872, China

⁵Department of Physics and Astronomy, University of Tennessee, Knoxville, Tennessee 37996, USA

(Dated: March 6, 2018)

We use single-crystal neutron diffraction to determine the crystal structure symmetry and the magnetic evolution in the rhodium doped iridates $\text{Sr}_2\text{Ir}_{1-x}\text{Rh}_x\text{O}_4$ ($0 \leq x \leq 0.16$). Throughout this doping range, the crystal structure retains a tetragonal symmetry (space group $I4_1/a$) with two distinct magnetic Ir sites in the unit cell forming staggered IrO_6 rotation. Upon Rh doping, the magnetic order is suppressed and the magnetic moment of Ir^{4+} is reduced from $0.21 \mu_B/\text{Ir}$ for $x = 0$ to $0.18 \mu_B/\text{Ir}$ for $x = 0.12$. The magnetic structure at $x = 0.12$ is different from that of the parent compound while the moments remain in the basal plane.

PACS numbers: 75.47.Lx, 75.25.-j, 61.05.F-, 71.70.Ej

The 5d-based iridates have attracted much attention due to the physics arising from the spin-orbit interaction (SOI). The enhanced SOI competes with other relevant energies, including the Coulomb interaction U and tetragonal crystalline electric field (CEF) energy Δ , and leads to a new set of energy balances that drive a large variety of quantum phases such as the effective $J_{\text{eff}} = 1/2$ Mott state,¹⁻³ the correlated topological insulator,⁴ a spin liquid in the hyperkagome structure,⁵ the Weyl semimetal with Fermi arcs,⁶ and the Kitaev relevant quantum compass model.^{7,8} Among all the iridates studied, the single layer Sr_2IrO_4 is considered a prototypical system and has been subjected to the most extensive investigations mainly because of the spin-orbit-induced insulating $J_{\text{eff}} = 1/2$ state. This state has been experimentally established by angle-resolved photoemission spectroscopy (ARPES) and resonant X-ray scattering measurements.^{1,3} The crystal and electronic structures bear key similarities to those of the celebrated cuprate La_2CuO_4 , such as the quasi-two-dimensional structure, effectively one hole per Ir/Cu ion, low energy magnetic excitations described by the antiferromagnetic (AF) Heisenberg model, large magnetic exchange interactions, and pseudogap-like state in the doped system.⁹⁻¹¹ By mapping the $J_{\text{eff}} = 1/2$ space, the electronic structure of Sr_2IrO_4 can be described by a $\text{SU}(2)$ invariant one band Hubbard model that is analogous to the cuprate and it is suggested that the superconducting phase can be induced by electron doping.¹²⁻¹⁴ In searching for novel superconductivity, it is found that the magnetic and electronic properties are highly sensitive to the substitution at the Sr, Ir or O sites.¹⁵⁻²⁰ For instance, doped $\text{Sr}_2\text{Ir}_{1-x}\text{Rh}_x\text{O}_4$ exhibits precipitous drops in both electrical resistivity and magnetic ordering temperatures in the regime of $0 \leq x \leq 0.16$ and evolves into an insulating state characterized by Anderson localization for larger Rh concentration ($0.24 \leq x \leq 0.85$), and finally crosses over

into a correlated metal at $x = 1$.²⁰ This indicates that chemical substitution can effectively alter the delicate balance between competing local energies and leads to exotic electronic ground states. Here, we report a single-crystal neutron diffraction study on $\text{Sr}_2\text{Ir}_{1-x}\text{Rh}_x\text{O}_4$ with $x \leq 0.16$. The crystal structure in this doping regime has a tetragonal symmetry of $I4_1/a$. The magnetic iridium ions reside on two inequivalent sites with distinct Ir-O bond distances. This doped system undergoes a change of its AF structure and a drastic reduction of its ordering temperature. The ordered moment decreases from $0.21 \mu_B/\text{Ir}$ at $x = 0$ to $0.18 \mu_B/\text{Ir}$ at $x = 0.12$. This study provides a crucial structural characterization that critically links to the in-plane AF order arising from magnetoelastic locking.

The $\text{Sr}_2\text{Ir}_{1-x}\text{Rh}_x\text{O}_4$ single crystals were grown using self-flux techniques.²¹ The Rh concentration is determined using both Energy Dispersion X-ray (EDX) and neutron diffraction using the single crystal diffractometer TOPAZ at the Spallation Neutron Source. Single crystals with dimension $\sim 0.5 \times 2 \times 2 \text{ mm}^3$ were chosen for diffraction studies. The temperature was controlled using a nitrogen cryocooler in the range from 100 to 300 K. Polarized and unpolarized neutron scattering were performed on the same samples using the triple axis spectrometers HB1 and HB1A at the High Flux Isotope Reactor with collimation of $48^\circ\text{-}80^\circ\text{-}80^\circ\text{-}240^\circ$ and $40^\circ\text{-}40^\circ\text{-}60^\circ\text{-}80^\circ$, respectively. Heusler crystals were used as monochromator and analyzer for the polarized neutron setup on HB1, a flipping ratio of 15 is achieved with incident neutron energy of 13.5 meV. A closed-cycle refrigerator was employed in measuring the T dependence of the magnetic and nuclear reflections for $4 < T < 300 \text{ K}$. The experiments of high resolution ($d_{\text{min}} = 0.5 \text{ \AA}$) single-crystal neutron diffraction were performed using time-of-flight Laue diffractometer TOPAZ. The data were collected on crystals with volume of approximately $1 \sim 1.5 \text{ mm}^3$ for 2

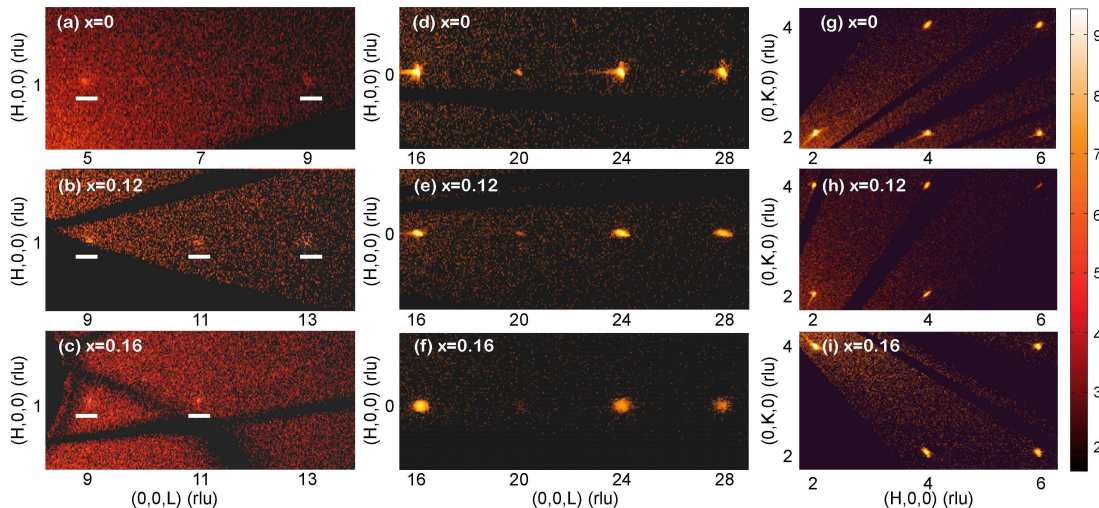


FIG. 1. (Color online) (a)-(c) Neutron diffraction pattern in the $(h, 0, l)$ scattering plane for $\text{Sr}_2\text{Ir}_{1-x}\text{Rh}_x\text{O}_4$ at $x=0, 0.12,$ and 0.16 . Note that the weak reflections appearing at $(\text{odd } h, 0, \text{odd } l)$ are highlighted. (d)-(f): Diffraction pattern in the $(0, 0, l)$ scattering plane, with only $(0, 0, 4n)$ reflections present. (g)-(i): pattern in the $(h, k, 0)$ scattering plane. Reflections at $(\text{odd } h, \text{odd } k, 0)$ are absent.

hours at every orientation, a total of approximately 24 hours for each crystal. Sample orientations were optimized with CrystalPlan²² for an estimated 98% coverage of symmetry-equivalent reflections of the tetragonal cell. The raw Bragg intensities were obtained using 3D ellipsoidal integration method.²³ Data reduction including Lorentz, absorption, TOF spectrum, and detector efficiency corrections were carried out with ANVRED3.²⁴ The reduced data were exported to the GSAS program suite²⁵ for wavelength dependent extinction correction and refined to convergence using SHELX97.²⁶

The parent compound was reported to have a tetragonal structure (SG $I4_1/acd$) from neutron powder diffraction.^{27,28} Recent single-crystal neutron diffraction studies have revealed a series of nuclear Bragg peaks which violate the reflection conditions of the reported space group and persist above the AF transition.^{29,30} Although the data suggest the lowering of crystal symmetry, the limited access to high-symmetry scattering planes using triple axis spectrometers prevents a definitive determination of the structure. To obtain a comprehensive characterization, we collected over six thousands nuclear reflections at TOPAZ for individual compositions ($x = 0, 0.12,$ and 0.16). Figure 1 compares the characteristic reciprocal space images as a function of Rh concentration at 100 K. Panels (a)-(c) show the map in the $(h, 0, l)$ plane, where peaks violating the reflection condition ($h, l = 2n$ for the $h0l$ family, where n is integer) in $I4_1/acd$ are clearly visible. The presence of weak peaks of $(1, 0, 5), (1, 0, 9)$ and $(1, 0, 11)$ in all samples is consistent with our previous report on the undoped Sr_2IrO_4 .²⁹ In addition, the presence of reflections $(0, 0, l)$ with $l = 4n$ indicates the samples retain a 4_1 -screw axis along the c -direction [panels (d)-(f)]. These observations

indicate that the crystal structure is reduced to either $I4_122$ or $I4_1/a$, nonisomorphic subgroups of $I4_1/acd$, due to the absent c - and d -glides. A close examination of the diffraction pattern in the $(h, k, 0)$ plane reveals missing reflections at $(\text{odd } h, \text{odd } k)$, as shown in Figs. 1(g)-1(i). Since $I4_122$ allows reflections with $h + k = 2n$ while $I4_1/a$ only permits peaks with $h, k = 2n$, the absence of these peaks strongly indicates that the parent and lightly Rh-doped Sr_2IrO_4 have a tetragonal $I4_1/a$ space group. This contrasts with the prevailing $I4_1/acd$ symmetry obtained from powder X-ray and neutron diffraction studies.^{27,28,31} For Sr_2IrO_4 with this crystal structure, the iridium atoms reside on two inequivalent sites Ir_1 and Ir_2 with different IrO_6 environments [Fig. 2(a)].

The correct description of crystal symmetry is critical to understand the underlying physical properties, *i.e.*, the robust locking of iridium moment with respect to the correlated rotation of oxygen octahedra found in both neutron and X-ray resonant scattering studies.^{29,32} A recent nonlinear optical rotational anisotropy spectrometer experiment has shown that the amplitude pattern of the second and third harmonic generation signals from Sr_2IrO_4 are well described by $4/m$ point group, and consistent with neutron diffraction results.³³ It was predicted by Jackeli and Khaliullin (JK) that the relationship between the moment canting angle ϕ and the octahedral rotation angle α depends on the strengths of SOI and the uniform tetragonal CEF distortion Δ .⁷ A perfect magnetoelastic locking ($\phi/\alpha \sim 1$) can only be achieved at $\Delta \sim 0$. However, the presence of unequal tetragonal distortion for individual Ir_1 and Ir_2 sites allows each sublattice to possess different spin and orbital compositions. The calculation incorporating staggered tetragonal splitting ($\Delta_1 = -\Delta_2$) on an extended JK model

does reproduce the experimental confirmation where the magnetic moment rigidly follows the IrO_6 rotation, despite a substantial noncubic distortion.^{33,34} Our diffraction work gives accurate experimental measurement of the unequal IrO_6 distortions. The relative change of Ir-O bond distances $\delta d/d$ for two iridium sites is on the order of 10^{-3} , sufficient to produce superlattice peaks for the structure symmetry determination. Our result emphasizes that the unequal tetragonal crystal field splitting Δ even with small magnitude is important to understand the magnetic order with in-plane moment. Both the Ir-O bond distance and Ir-O-Ir bond angle remain essentially unchanged with increasing Rh content, [Table I]. This suggests that the modification in local environment around the iridium ions is not responsible for the suppression of the electrical resistivity and the AF order. Instead, the enhanced conduction may be attributed to carrier doping or reduction of SOI, or both, in the Rh doped Sr_2IrO_4 .^{20,35}

TABLE I. Structural parameters of $\text{Sr}_2\text{Ir}_{1-x}\text{Rh}_x\text{O}_4$ ($x = 0, 0.12, 0.16$) using SG $I4_1/a$ at $T = 100$ K. Two inequivalent Ir_1 (Wyckoff position 4a) and Ir_2 (4b) are located at $(0, 1/4, 1/8)$ and $(0, 1/4, 5/8)$, respectively. Two Sr_1 and Sr_2 atoms (8e) are at $(0, 1/4, z)$. The apical oxygen atoms O_1 and O_2 (8e) are at $(0, 1/4, z)$ and the in-plane O_3 (16f) at (x, y, z) . The out-of-plane and in-plane Ir-O bond distances and in-plane Ir-O-Ir bond angles are listed.

	$x = 0$	$x = 0.12$	$x = 0.16$
$a(\text{\AA})$	5.485(1)	5.477(1)	5.477(1)
$c(\text{\AA})$	25.775(1)	25.791(1)	25.767(1)
$V(\text{\AA}^3)$	775.51(3)	773.68(4)	773.17(3)
$\text{Sr}_1(z)$	0.30043(3)	0.30047(4)	0.30046(4)
$\text{Sr}_2(z)$	0.44959(3)	0.44952(4)	0.44951(4)
$\text{O}_1(z)$	0.20479(4)	0.20479(5)	0.20476(5)
$\text{O}_2(z)$	0.54520(4)	0.54519(5)	0.54525(5)
$\text{O}_3(x)$	0.1987(1)	0.1992(1)	0.1997(2)
$\text{O}_3(y)$	0.9485(1)	0.9493(2)	0.9497(2)
$\text{O}_3(z)$	0.1250(1)	0.1250(1)	0.1250(1)
$\text{Ir}_1\text{-O}_1(\text{\AA})$	2.056(1)	2.058(1)	2.055(1)
$\text{Ir}_2\text{-O}_2(\text{\AA})$	2.057(1)	2.058(1)	2.055(1)
$\text{Ir}_1\text{-O}_3(\text{\AA})$	1.981(1)	1.975(1)	1.975(1)
$\text{Ir}_2\text{-O}_3(\text{\AA})$	1.979(1)	1.977(1)	1.975(1)
$\text{Ir}_1\text{-O}_3\text{-Ir}_2(^{\circ})$	156.74(5)	157.05(5)	157.24(6)

Sr_2IrO_4 forms a canted AF configuration below $T_N \approx 225$ K with magnetic propagation wavevector $\vec{q}_m = (1, 1, 1)$. With Rh doping, T_N is quickly suppressed and the magnetization decreases accordingly. Figure 3 shows the diffraction result at $x = 0.12$. The magnetic scattering appears at position $(1, 0, 2n+1)$, different from that of the undoped sample at $(1, 0, 4n)$ or $(0, 1, 4n+2)$. The intensity of the strongest $(1, 0, 3)$ peak decreases smoothly on warming and levels off to a T -independent background above $T_N = 110$ K, where the magnetization

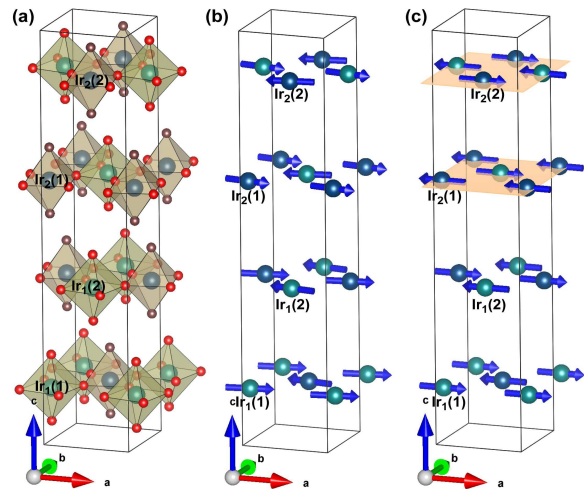


FIG. 2. (Color online) (a) The crystal structure of $\text{Sr}_2\text{Ir}_{1-x}\text{Rh}_x\text{O}_4$ with SG $I4_1/a$ (Sr ions are skipped for clarity). Two inequivalent Ir atoms at $(0, 1/4, 1/8)$ and $(0, 1/4, 5/8)$ are labeled as Ir_1 (green) and Ir_2 (blue), the other Ir ions are generated by the symmetry operations. (b) The canted AF structure with $\vec{q}_m = (1, 1, 1)$ for undoped Sr_2IrO_4 where the components form a staggered $\downarrow\uparrow\downarrow$ pattern along the c axis. (c) The AF configuration with $\vec{q}_m = (0, 0, 0)$ for the $x = 0.12$ sample. Note that the spins in the top two layers change directions compared to panel (b).

also disappears.²⁰ The magnetic transition is significantly rounded and different from the undoped sample. The scattering at wavevector of $(1, 0, 2n+1)$ has mixed contributions from either magnetic or allowed nuclear scattering in SG $I4_1/a$. Polarized neutron analysis at the HB1 spectrometer is employed to elucidate the nature of those reflections. Fig. 3(b) compares scans across the $(1, 0, 3)$ peak at 4 K in the spin-flip (SF) and non-spin-flip (NSF) channels with $\vec{P} \parallel \vec{Q}$, where \vec{P} is the neutron polarization vector and \vec{Q} the momentum transfer. The scattering cross section in the SF channel is purely magnetic if one neglects contributions from nuclear spins and imperfect neutron polarization. Albeit weak, the peak is clearly visible compared to data in the NSF channel, where the cross section involves only the nuclear scattering process. This confirms that the T -dependence of $(1, 0, 3)$ seen from unpolarized neutrons is indeed magnetically contributed. Fig. 3(c) further compares the polarization analysis of the $(1, 0, 1)$ Bragg peak. The stronger, well defined peak profile in the NSF channel verifies that this reflection is dominated by nuclear scattering.²⁹

These observations identify a magnetic structure with vector $\vec{q}_m = (0, 0, 0)$. There are two possible configurations: (1) identical to Sr_2IrO_4 in an external magnetic field,³ and (2) similar to the Mn- or Ru-doped system where the magnetic moments point along the c -axis.^{19,36} In principle, the polarized neutron diffraction with $\vec{P} \perp \vec{Q}$ will provide the moment direction since the bulk magnetization measurement offers no conclu-

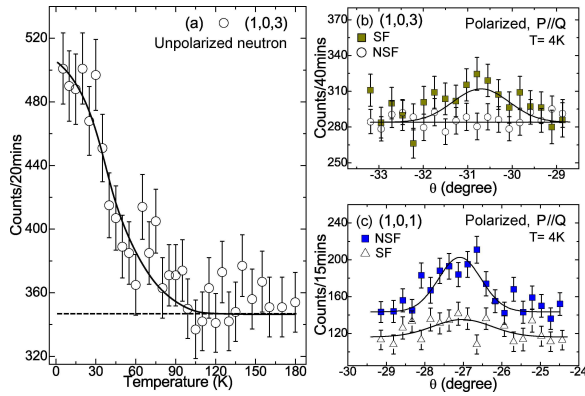


FIG. 3. (Color online) The T -dependence of the (1,0,3) peak intensity measured with unpolarized neutron for $\text{Sr}_2\text{Ir}_{0.88}\text{Rh}_{0.12}\text{O}_4$. Note that the considerable rounding near the transition. The solid line is guide to the eye, and the dashed line represents T -independent background. (b) The (1,0,3) rocking scans in the SF and NSF channels with $\vec{P} \parallel \vec{Q}$ at 4 K. (c) The (1,0,1) rocking scans in the NSF and SF channels with $\vec{P} \parallel \vec{Q}$ at 4 K.

sive determination of the magnetic easy axis. However, the counting statistics are severely affected by the reduced flux of polarized neutrons and the small sample size. We resolved the magnetic structure by quantitatively analyzing the unpolarized diffraction intensities. The magnetic structure with two magnetic $\text{Ir}_{1,2}$ ions can be decomposed into one dimensional irreducible representation $\Gamma_{\text{mag}}(1, 2) = \Gamma_1 + \Gamma_4 + \Gamma_5 + \Gamma_6 + \Gamma_7 + \Gamma_8$ from symmetry analysis software BasReps.³⁷ The six basis vectors complete the total magnetic degrees of freedom within the unit cell. $\Gamma_{1,4}$ describe spin configurations with a c -axis moment and $\Gamma_{5,6}/\Gamma_{7,8}$ illustrate in-plane magnetic structures with the moment along the a or b directions. As the magnetic cross section is proportional to the spin component perpendicular to the wavevector transfer $\vec{S}_{\perp} = \hat{Q} \times (\vec{S} \times \hat{Q})$, one expects scattering intensities for the magnetic structure with the c -axis moment to decrease more rapidly with increasing L -indices. Fig. 4 displays the rocking scans across $(1, 0, 2n + 1)$ reflections showing dominant magnetic scattering at low temperature. The inset compares the observed intensities with calculation from two magnetic models. The data are clearly better described by the one with the moment aligned along the a -axis. An ordered magnetic moment of $0.18(1) \mu_B/\text{Ir}$ at $T = 4$ K is obtained assuming that the magnetic scattering arises solely from the Ir ions. A key finding revealed in the magnetic structure [Fig. 2(c)] is that the moments in the top two layers of IrO_6 reverse their directions compared with parent compound. This underscores how the interlayer magnetic correlations change upon Rh-doping.

Although it is predicted that a spin reorientation transition exists for tetragonal distortion greater than a critical value $\Delta_c \approx 190$ meV,⁷ the structural refinement reveals no changes in either the crystal structure symmetry

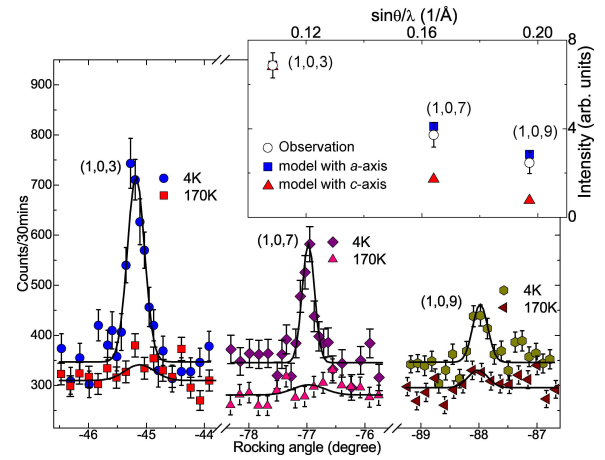


FIG. 4. (Color online) Comparison of the rocking scans across the (1,0,3), (1,0,7), and (1,0,9) reflections at 4 K and 170 K for $\text{Sr}_2\text{Ir}_{0.88}\text{Rh}_{0.12}\text{O}_4$. Inset shows the observed integrated magnetic intensities (open circle) versus spin configurations with in-plane moment (blue square) and out-of-plane moment (red triangle). Calculated intensities of two models are normalized to the (1,0,3) reflection.

or the tetragonal distortion for the Rh content studied. It is not surprising that the magnetic moments remain in the ab plane. The aforementioned unequal tetragonal distortion for Ir_1/Ir_2 from $I4_1/a$ symmetry may play a role for the locked in-plane moment. Furthermore, the variational Monte Carlo method has shown that the introduction of the Hund's coupling enhances the anisotropy and the in-plane AF structure becomes more energetically favorable.³⁸ On the other hand, a moment reorientation transition was reported in Mn-doped Sr_2IrO_4 , where moments orient along the c -axis. The flop of spin orientation might originate from the quenched Mn moments with c -axis single ion anisotropy. Likewise, the noncubic crystal field could also be enhanced due to larger lattice mismatch between $3d$ and $5d$ transition metal ions.

The change of magnetic propagation wavevector has been commonly observed in Sr_2IrO_4 from perturbations such as chemical (Ru/Mn)-doping or magnetic field. The small insulating gap ≤ 0.6 eV^{2,39-41} observed in the pure system suggests it is in the vicinity of the metal-insulator transition.^{1,42,43} Indeed, the chemical substitution has shown a profound effect on the electronic properties.^{17,18,20,44} In the case of rhodium doping, it was initially assumed that Rh ions were isovalent substitution at the Ir sites, (*i.e.*, Rh^{4+} substitutes for Ir^{4+}). The reduction in resistivity was thought to be a result of the weakened SOI due to Rh doping. In addition, the staggered AF field associated with the magnetic order lifts the degeneracy along the edge of the Brillouin zone and opens up a finite magnetic gap.³⁸ Thus, the vanishing magnetic order observed in the Rh-doped Sr_2IrO_4 would account for the insulator-metal crossover. However, the picture of isovalent Rh substitution has been challenged by recent ARPES studies.³⁵ Cao *et al.* reported that the

top of the valence band moves up with Rh doping and forms a hole pocket at the $(\pi, 0)$ point, contrasting with the 180 meV gap below the Fermi surface at $x = 0$. This result shows that Rh atoms effectively act as hole dopants and cause a distribution of Ir^{4+} and Ir^{5+} . Since the splitting between the $J_{\text{eff}} = 1/2$ and $J_{\text{eff}} = 3/2$ becomes smaller with decreasing SOI strength in the lighter Rh atoms, the Rh substitutions would lead to the hopping of an electron from the Ir to the neighboring Rh site as the free energy becomes lower. The change of Ir oxidation state is independently verified by the shift of white line peak position from Rh and Ir L_3 edges of the X-ray absorption spectroscopy.⁴⁵ If the effective hole doping is taken into account, the ordered moment of the magnetic iridium would become even smaller. The reduced moment value is similar to that of other iridates,^{29,30,36,46} reflecting the large itinerancy of iridium electrons and the covalency between the $5d$ and ligand orbitals. Interestingly, the system remains a robust spin-orbit coupled state even though Rh has a considerably smaller SOI strength (0.16 eV compared to 0.4 eV for Ir), as evidenced by the large L_3/L_2 intensity ratio from the X-ray absorption spectroscopy.

In summary, single-crystal neutron diffraction clarifies the global structural symmetry of the Rh doped $\text{Sr}_2\text{Ir}_{1-x}\text{Rh}_x\text{O}_4$ ($0 \leq x \leq 0.16$) belongs to a lower $I4_1/a$ space group. The identification of two distinct magnetic Ir sites is relevant to the canted AF order where the moments rigidly follow the rotation of the IrO_6 octahedra even in the presence of substantial tetragonal distortion. This study further reveals that the magnetic order observed in Sr_2IrO_4 is suppressed upon Rh doping and is transformed into a different in-plane AF configuration with reduced moment of $0.18(1) \mu_B/\text{Ir}$ at $x = 0.12$. The crystal and magnetic structures are essential to understand the detailed spin and orbital composition of the ground state and the robustness of a $J_{\text{eff}} = 1/2$ description in this archetype spin-orbit entangled system.

We thank Dr. Yue Cao and David Hsieh for invaluable discussions. Research at ORNL's HFIR and SNS was sponsored by the Scientific User Facilities Division, Office of Basic Energy Sciences, U.S. Department of Energy. The work at University of Kentucky was supported by NSF through grants DMR-0856234 and DMR-1265162. J.C. Wang acknowledges support from China Scholarship Council.

-
- ¹ B. J. Kim *et al.*, Phys. Rev. Lett. **101**, 076402 (2008).
² S. J. Moon *et al.*, Phys. Rev. B **80**, 195110 (2009).
³ B. J. Kim *et al.*, Science **323**, 1329 (2009).
⁴ A. Shitade *et al.*, Phys. Rev. Lett. **102**, 256403 (2009).
⁵ Y. Okamoto, M. Nohara, H. Aruga-Katori, and H. Takagi, Phys. Rev. Lett. **99**, 137207 (2007).
⁶ X. G. Wan, A. M. Turner, A. Vishwanath, and S. Y. Savrasov, Phys. Rev. B **83**, 205101 (2011).
⁷ G. Jackeli and G. Khaliullin, Phys. Rev. Lett. **102**, 017205 (2009).
⁸ Y. Singh *et al.*, Phys. Rev. Lett. **108**, 127203 (2012).
⁹ J. Kim *et al.*, Phys. Rev. Lett. **108**, 177003 (2012).
¹⁰ Y. J. Yan *et al.*, arXiv:1506.06557 (2015).
¹¹ Y. K. Kim, N. H. Sung, J. D. Denlinger, and B. J. Kim, arXiv:1506.06639 (2015).
¹² F. Wang and T. Senthil, Phys. Rev. Lett. **106**, 136402 (2011).
¹³ Y. Z. You, I. Kimchi, and A. Vishwanath, Phys. Rev. B **86**, 085145 (2012).
¹⁴ H. Watanabe, T. Shirakawa, and S. Yunoki, Phys. Rev. Lett. **110**, 027002 (2013).
¹⁵ S. Chikara *et al.*, Phys. Rev. B **80**, 140407 (2009).
¹⁶ O. B. Korneta *et al.*, Phys. Rev. B **82**, 115117 (2010).
¹⁷ M. Ge *et al.*, Phys. Rev. B **84**, 100402 (2011).
¹⁸ J. S. Lee, Y. Krockenberger, K. S. Takahashi, M. Kawasaki, and Y. Tokura, Phys. Rev. B **85**, 035101 (2012).
¹⁹ S. Calder *et al.*, Phys. Rev. B **86**, 220403 (2012).
²⁰ T. F. Qi *et al.*, Phys. Rev. B **86**, 125105 (2012).
²¹ G. Cao, J. Bolivar, S. McCall, J. E. Crow, and R. P. Guertin, Phys. Rev. B **57**, 11039 (1998).
²² J. Zikovsky *et al.*, J. Appl. Cryst. **44**, 418 (2011).
²³ A. J. Schultz *et al.*, J. Appl. Cryst. **47**, 915 (2014).
²⁴ A. J. Schultz *et al.*, J. Am. Chem. Soc. **106**, 999 (1984).
²⁵ A.C. Larson and R.B. Von Dreele, "General Structure Analysis System (GSAS)", Los Alamos National Laboratory Report LAUR 86-748 (1994).
²⁶ G. Sheldrick, Acta Cryst. A **64**, 112 (2008).
²⁷ Q. Huang *et al.*, J. Solid State Chem. **112**, 355 (1994).
²⁸ M. K. Crawford *et al.*, Phys. Rev. B **49**, 9198 (1994).
²⁹ F. Ye *et al.*, Phys. Rev. B **87**, 140406 (2013).
³⁰ C. Dhital *et al.*, Phys. Rev. B **87**, 144405 (2013).
³¹ T. Shimura, Y. Inaguma, T. Nakamura, M. Itoh, and Y. Morii, Phys. Rev. B **52**, 9143 (1995).
³² S. Boseggia *et al.*, J. Phys. Condens. Matter **25**, 422202 (2013).
³³ D. H. Torchinsky *et al.*, Phys. Rev. Lett. **114**, 096404 (2015).
³⁴ N. B. Perkins, Y. Sizyuk, and P. Wolffe, Phys. Rev. B **89**, 035143 (2014).
³⁵ Y. Cao *et al.*, arXiv:1406.4978 (2014).
³⁶ S. Calder *et al.*, arXiv:1508.01807 (2015).
³⁷ J. Rodriguez-Carvajal, Physica B **192**, 55 (1993).
³⁸ H. Watanabe, T. Shirakawa, and S. Yunoki, Phys. Rev. Lett. **105**, 216410 (2010).
³⁹ K. Ishii *et al.*, Phys. Rev. B **83**, 115121 (2011).
⁴⁰ Q. Li *et al.*, Scientific Reports **3**, 3073 (2013).
⁴¹ J. Dai, E. Calleja, G. Cao, and K. McElroy, Phys. Rev. B **90**, 041102 (2014).
⁴² S. J. Moon *et al.*, Phys. Rev. Lett. **101**, 226402 (2008).
⁴³ Q. Wang *et al.*, Phys. Rev. B **87**, 245109 (2013).
⁴⁴ X. Chen *et al.*, Phys. Rev. B **92**, 075125 (2015).
⁴⁵ J. P. Clancy *et al.*, Phys. Rev. B **89**, 054409 (2014).
⁴⁶ F. Ye *et al.*, Phys. Rev. B **85**, 180403 (2012).